Bioactive Materials 47 (2025) 198–208

Contents lists available at ScienceDirect

Bioactive Materials

journal homepage: www.keaipublishing.com/en/journals/bioactive-materials

Injectable iodine-containing peptide hydrogel for treatment of MRSA infection

Yu Zhang [a,b,1], Haiyan Liu [c,1], Weiqi Zhang [c], Yinghao Ding [b], Shengyi Zhang [b], Xiaowan Huang [c], Jiali Chen [a,**], Zhimou Yang [a,b,*], Feng Lin [c,***]

[a] Zhejiang Key Laboratory of Intelligent Cancer Biomarker Discovery and Translation, Department of Gastrointestinal Surgery, The First Affiliated Hospital, Wenzhou Medical University, Wenzhou, Zhejiang Province, 325035, PR China
[b] State Key Laboratory of Medicinal Chemical Biology, College of Life Sciences, Nankai University, Tianjin, 300071, PR China
[c] Department of Gynecology, The First Affiliated Hospital, Wenzhou Medical University, Wenzhou, Zhejiang Province, 325035, PR China

ARTICLE INFO

Keywords:
Iodine
Peptide
Self-assembly
Antibacterial
Endometritis

ABSTRACT

Iodine is widely acknowledged for its potent antimicrobial properties. However, its clinical utility is often hampered by its unsatisfactory stability, uncontrolled release of active iodine and toxicity in moist environments. In this study, we report a novel iodine-containing hydrogel (I_2@Nap-FFGP) designed for sustained iodine delivery under humid physiological and pathological conditions. I_2@Nap-FFGP was fabricated using a self-assembling peptide-based hydrogel containing a proline motif to form a stable iodine complex. The resulting hydrogel exhibited excellent biocompatibility and robust antibacterial effect, it significantly inhibited bacteria-associated endometrial infections in mice and effectively alleviated inflammation. Moreover, the hydrogel successfully restored endometrial architecture and function. Notably, I_2@Nap-FFGP remarkably improved pregnancy rates in mice with endometritis owing to its therapeutic effects. Our findings highlight the potential of this innovative hydrogel system for stable iodine application under humid and aqueous physiological conditions, offering a promising platform for future antibacterial therapies in clinical settings.

1. Introduction

Iodine is an essential trace element vital for biological activities and organic structures in humans, with 70–80 % present in the thyroid [1]. It plays a crucial role in the synthesis of thyroid hormones, which are important for enhancing metabolism and promoting growth and development, particularly in the brain [2]. In addition to its biological functions, iodine is widely used for its antibacterial properties, as it exhibits unique physiochemical characteristics that allow for rapid penetration and destruction of cell walls, oxidation of proteins and enzymes, and disturbance of DNA [3]. Among the various iodic agents, povidone–iodine (commercially known as Iodophor or PVP-I), a complex formed between polyvinylpyrrolidone (PVP) and iodine [4,5], is one of the most popular choices. Owing to its broad-spectrum antibacterial activity, high efficiency, and low cost, PVP-I is extensively used in clinical and domestic applications for disinfecting hands, skin, medical apparatus, and instruments [6–8]. However, despite the evidence that PVP significantly enhances the stability and durability of iodine in antibacterial applications, the uncontrolled release of iodine can potentially be toxic, limiting the effectiveness of PVP-I as a disinfectant [9,10]. Most importantly, the poor stability and retention of PVP-I due to its high water solubility are particularly undesirable in the physiologically widespread humid and aqueous environments of deep-seated tissues and foci, such as the uterus [11]. Therefore, there is an urgent need to develop effective methods for iodine loading and release to meet clinical demands.

Recent advancements in nanoscience and nanomedicine have provided novel strategies for establishing efficient and biosafe antibacterial therapies [12,13]. For instance, poly(N-vinyl-2-pyrrolidone-co-methyl methacrylate), which contains a pyrrolidone motif, has been designed

* Corresponding author. Zhejiang Key Laboratory of Intelligent Cancer Biomarker Discovery and Translation, Department of Gastrointestinal Surgery, The First Affiliated Hospital, Wenzhou Medical University, Wenzhou, Zhejiang Province, 325035, PR China.
** Corresponding author.
*** Corresponding author.
E-mail addresses: chenjl@wmu.edu.cn (J. Chen), yangzm@nankai.edu.cn (Z. Yang), linfeng@wmu.edu.cn (F. Lin).
[1] Authors contributed equally to this work.

https://doi.org/10.1016/j.bioactmat.2025.01.010
Received 5 November 2024; Received in revised form 9 January 2025; Accepted 11 January 2025

to form PVP-I-like antibacterial iodine–polymer complex nanoparticles that exhibit excellent antibacterial stability while retaining water solubility [14]. Metal-organic framework (MOFs) have also been employed for iodine absorption, serving as both storage reservoirs and delivery platforms for biocidal iodine [15]. Iodine-loaded MOFs can be incorporated into biodegradable polymers for applications such as door-handle covers, which can completely inhibit the transmission of Gram-positive and Gram-negative bacteria as well as fungi under realistic touching conditions. Hydrogels have also been investigated for iodine loading and release; a cryogel mixture of bacterial cellulose, gelatin, and dopamine was shown to effectively produce I_2 and sodium iodides in situ through the reduction of sodium [16]. Nevertheless, current iodic sterilizing agents remain primarily confined to topical applications such as for instrument sterilization and the treatment of skin or mucous membrane infections [17]. This limitation is largely owing to concerns regarding their stability and biocompatibility, which restrict their effectiveness in broader applications.

Recently, short peptide-based hydrogels have attracted considerable attention owing to their excellent biocompatibility, controllable chemical structures, unique constructive units, and ability to accommodate various functional modifications [18]. In particular, supramolecular self-assembly has emerged as an effective strategy for constructing reliable soft-peptide biomaterials [19–22]. The inherently water-rich environment of hydrogels may be crucial for application in physiologically humid and aqueous pathological conditions [23]. Thus, we hypothesized that a well-defined self-assembling peptide hydrogel based on rational sequence design and construction could serve as a stable and effective iodic agent.

Inspired by the interaction between PVP and iodine, we proposed that proline (Pro), which has a similar pyrrolidone structure to PVP, could also form a complex with iodine. Accordingly, we designed a short peptide as a self-assembling agent and used a simple heating–cooling method to fabricate an iodine-complexed hydrogel for the treatment of endometrial infections (Scheme 1). The assembling factor contained two major components: (i) a pro motif for iodine complexation, and (ii) an assembly sequence based on naphthalene–diphenylalanine. The resulting peptide hydrogel exhibited excellent antibacterial efficacy, reduced the inflammation in mouse endometria by inhibiting pathogenic bacteria, and improved the pregnancy rate of mice with endometritis. Overall, this hydrogel provides a promising platform for the application of iodine under humid and aqueous physiological conditions.

2. Experimental section

2.1. Synthesis of peptide

Peptides were synthesized via solid phase peptide synthesis (SPPS) using 2-chlorotrityl chloride resin and corresponding Fmoc-protected amino acids. The synthetic route and molecular structure were shown below. High-performance liquid chromatography (HPLC, Agilent, US) was employed for purification using a reverse phase C18 column (Waters, RP18 10.0 μm, 19 × 150 mm). The purified peptides were lyophilized and characterized by LC-MS.

2.2. Cell culture

Endometrial stromal cells were obtained from Pricella (Wuhan, China) and cultured in DMEM/F12 (Gibco) with 10 % fetal bovine serum (Gibco), 100 U/mL penicillin (Gibco), and 100 μg/mL streptomycin (Gibco). The cells were incubated at 37 °C with 5 % CO_2 for culture and passage unless otherwise stated.

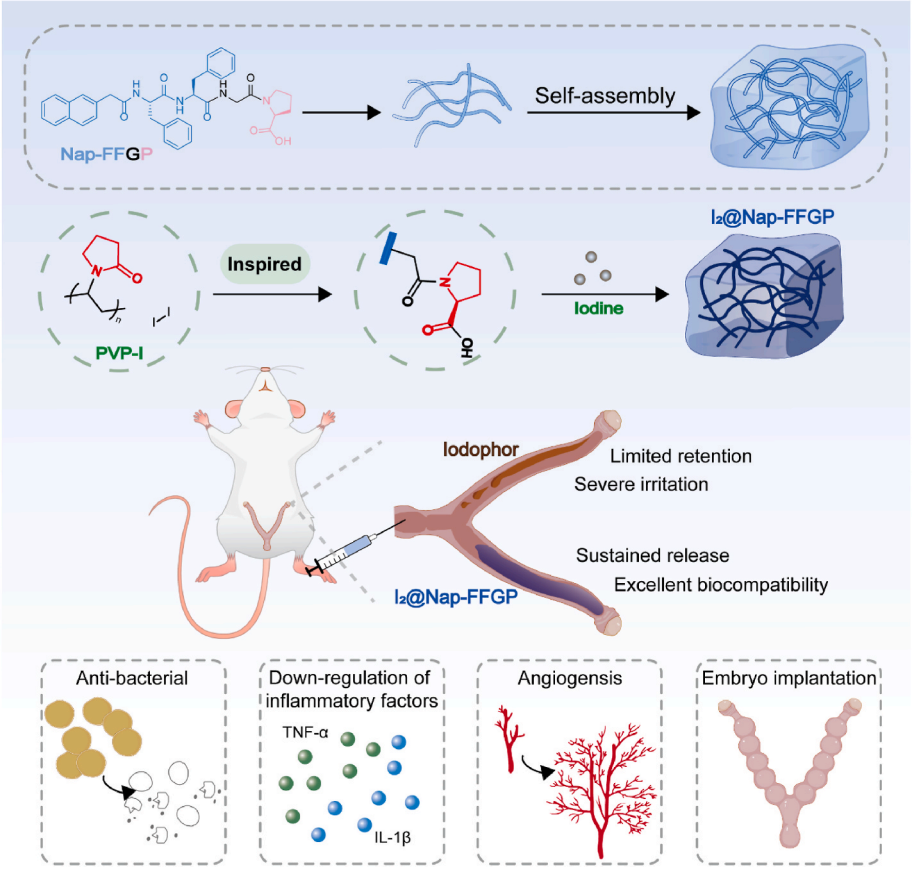

Scheme 1. Schematic illustration of injectable I_2@Nap-FFGP hydrogel for the treatment of endometrial infection.

2.3. Bacterial culture

Methicillin-resistant *Staphylococcus aureus* (USA 300) was cultured in Luria-Bertani (LB) broth and agar. The strains were restored at −80 °C before testing. The strains were melted to room temperature quickly and inoculated in culture medium at 1:100 vol ratio (10 ml) for a duration of 16–20 h. The absorption at 600 nm (O.D. 600) was used to monitor the growth of bacteria. Subsequently, the cells were collected by centrifugation at a speed of 5000 rpm (25 °C) for 5 min. To prepare the liquid culture medium, powder of the culture mediums was dissolved into a solution and sterilized at 121 °C with a high pressure for about 1 h and then cooled down to room temperature.

2.4. Preparation and characterization of peptidic and iodine-containing hydrogel

Heating-cooling method was employed to prepare the hydrogel. Generally, Nap-FFGP was dissolved in PBS buffer (3 mg/mL) while the pH was adjusted to 7. Then the solution was heated to 80 °C for complete dissolution of Nap-FFGP and then cooled to room temperature for the formation of Nap-FFGP hydrogel.

For iodine-containing hydrogel, iodine was firstly dissolved in anhydrous ethanol to form a stock solution (100 mg/mL), which was subsequently added to the prepared Nap-FFGP solution at 80 °C and flowed by cooling to room temperature to form I_2@Nap-FFGP hydrogel. Except for specific mentions, the concentration of peptide in all samples were 3 mg/mL, while the concentration of iodine was 1 mg/mL.

The morphologies of all the samples were characterized by TEM images. Generally, the hydrogel was dropped onto carbon-coated grids and stained with 2 % uranyl acetate for 1 min while iodine-containing hydrogel were not stained. Then the samples were washed once with deionized water and the images were captured by TEM.

2.5. Oscillatory rheological test

The samples of hydrogels (2 mg/mL) were measured on ARES-G2 Rheometer (TA Waters, USA) at 25 °C, with a 25 mm diameter plate and 0.5 mm gap. 1 % and 100 % strains were set for alternating cycles.

2.6. Critical micelle concentration

To measure the critical micelle concentration (CMC), Rhodamine 6G was introduced into peptide solutions with a final concentration at 5 μM and incubated at room temperature for 24 h. The maximum absorption wavelength (λ_{max}) of Rhodamine 6G was then recorded using a Microplate Reader to calculate the CMC.

2.7. In vitro release of iodine

A vial of I_2@Nap-FFGP hydrogel (1 mL) was placed in a water bath at 37 °C and subsequently immersed with 1 mL preheated PBS (pH 7.4) containing 1 wt% potassium iodide. At predetermined time points, 0.8 mL of the surrounding medium was collected and replaced with an equal volume of fresh medium. The release of iodine was measured by the absorbance of collected medium at 350 nm using a Microplate Reader.

2.8. Antibacterial test

To investigate the antibacterial effect against *Methicillin-resistant Staphylococcus aureus* (MRSA, USA300), MRSA (10^8 CFU/mL) were firstly collected and washed with PBS for three times, then the bacterial solution was mixed with the equal value of Nap-FFGP (3 mg/mL), I_2@Nap-FFGP, I_2@Nap-FFGA (3 mg/mL) and iodophor (1 mg/mL) respectively. The population of MRSA was quantified by plate counting over time to monitor the antibacterial effect.

2.9. Morphological changes of MRSA

MRSA were incubated with different samples at 37 °C for 4 h, collected by centrifugation and additional washes with PBS for three times. Then the MRSA were fixed and stored at 4 °C overnight. The fixed bacteria were washed with a buffer solution consisting of 0.1 M PB/Cacodylate for three times and stained with 1 % osmic acid for 1 h followed by another round of washing. After dehydrating by an ethanol gradient process, vacuum-dried, and finally sputter-coated with gold, the morphology was subsequently collected by SEM images.

2.10. Biofilm clearance experiment

This test was conducted on an aseptic transparent 96-well plate. After three days of incubation, the upper biofilm was removed, and the wells were washed with PBS. Following, 100 μL of different samples were added. After 4 h of incubation, the supernatant was discarded. The wells were washed three times with PBS, followed by the addition of 100 μL of 0.1 % crystal violet solution for staining for 10 min 100 μL of ethanol was added to dissolve the crystal violet. The optical density values at 595 nm were measured to detect the biofilm clearance.

2.11. Live/dead staining

Live/Dead staining was performed to visualize biofilm elimination. For biofilm CLSM imaging, SYTO 9 (485/498 nm) and propidium iodide (PI, 535/617 nm) fluorescent probes were used to distinguish between live and dead cells, where the live bacteria were presented as green fluorescence and red fluorescence indicated the dead species.

2.12. Cytotoxicity of I_2@Nap-FFGP

The cytotoxicity of the hydrogel was detected by 3-(4,5-Dimethylthiazol-2-yl)-2,5-diphenyltetrazolium bromide (MTT) assay according to the commercial protocol. Endometrial stromal cells were seeded in a 96-well plate with a density of 1×10^4 cells per for 24 h. I_2@Nap-FFGP hydrogel and iodophor were incubated in culture medium respectively (volume ratio was 1:4) for 24 h to prepare the infiltration solutions. Then, the culture medium was removed by infiltration solutions and incubated for another 24 h. Afterward, 10 μL MTT solution (5 mg/mL in PBS) was added into each well and co-incubated for another 4 h. The culture medium was then removed. 100 μL SDS-HCl solution (10 % SDS + 0.01 M HCl) was added to each well, and incubated overnight at 37 °C. Absorbance at 595 nm was measured using a Microplate Reader (Varioskan Lux, ThermoFisher, USA). Each sample was set up with three parallels.

Subsequently, the Live/Dead cell imaging kit (ThermoFisher, USA) was used to further measure the *in vitro* cytotoxicity of I_2@Nap-FFGP. Briefly, endometrial stromal cells (5×10^4 cells/well) were seeded in confocal dishes and cultured over 12 h. Then, 1 mL of the different infiltration solutions was added to the confocal dishes, respectively. After 24 h of incubation, the cells were rinsed twice with PBS (pH 7.4), and the Live/Dead cell imaging kit was added for staining, which co-incubated for about 15 min. Finally, images were captured using a confocal laser scanning microscope (CLSM, Leica Stellaris 5). Green fluorescence (Calcein AM) indicated live cells while dead cells represented as red fluorescence (BOBO-3 Iodide).

2.13. Hemolysis assay

Hemolysis assays were conducted using fresh mouse blood, which was centrifuged at 3000 rpm for 5 min, then washed with PBS for three times, and suspended at an 8 % concentration. A total amount of 100 μL of the prepared infiltration solutions was mixed with the red blood cell suspension (infiltration/blood suspension = 1/1, v/v) and incubated at 37 °C for 3 h. Triton X-100 was employed as positive control and PBS

was set as negative control. The samples were then collected by centrifugation at 3000 rpm for 5 min 100 μL supernatant was collected for measurement of absorbance at 570 nm using a Microplate Reader.

2.14. In vitro degradation

Simulated uterine fluid was employed for the test of biodegrading ability. I_2@Nap-FFGP hydrogel was incubated with equal volume of simulated uterine fluid at 37 °C water bath for 10 days. The hydrogel images in the vial were captured on days 1, 2, 3, 5, 7 and 10. For clearer observation of the hydrogel degradation, we removed the supernatant and inverted the glass vial in front of a blue background to capture optical images on Days 7 and 10. The composition of the simulated uterine fluid is provided in the Supplementary Table.

2.15. In vivo therapeutic effect

Animal experimental protocols were approved by the First Affiliated Hospital of Wenzhou Medical University (WYYY-AEC-2024-004). Female ICR mice (8 weeks) were fed in laminar flow cabinets under specific pathogen-free condition with randomly provided food and water. After anesthetizing the mice, they were inverted for 2 min to allow abdominal organs to shift into the thoracic cavity, fully extending the uterus. A micro-injector was inserted into the uterine cavity via the vagina, and 60 μL of *Staphylococcus aureus* suspension (OD = 0.95) was injected into each mouse. After injection, the speculum was removed, and the mice were inverted for another 2 min to ensure thorough contact of the bacterial solution with the uterine wall, allowing for vaginal constriction to prevent leakage. Mice in the control group received the same procedure with physiological saline. Twenty-four hours post-modeling, the mice were randomly divided into six groups for different set of experiments: Group 1, healthy mice without any treatment; Group 2, mice injected with PBS (100 μL); Group 3, mice injected with Nap-FFGP hydrogel (100 μL 3 mg/mL); Group 4, mice injected with I_2@Nap-FFGA hydrogel (100 μL 3 mg/mL, containing 1 mg/mL iodine); Group 5, mice injected with I_2@Nap-FFGP hydrogel (100 μL 3 mg/mL, containing 1 mg/mL iodine); Group 6, mice injected with Iodophor (100 μL). After 24 h of treatment, the mice were euthanized and the uterus and major organs were collected for further analysis.

To access the improved fertility, after 24 h of treatment, the female mice were caged together with male for 14 days. After that, the uteri were collected and the number of embryos were quantified.

2.16. RT-qPCR assay

To evaluate the levels of inflammatory-related mRNA expression in uterine tissues after different treatments, the total RNA was extracted with TRIzol (Thermo Fisher, USA) and subsequently quantified and purified. Then cDNA was prepared using HiScript IV All-in-One Ultra RT SuperMix (Vazyme, China). The real-time quantitative polymerase chain reaction (RT-qPCR) was then performed subsequently using ChamQ Universal SYBR qPCR Master Mix (Vazyme, China). The relative expression of mRNA was normalized to the expression level of GAPDH.

2.17. Statistical analysis

Data performed as indicated were presented as means ± SD, while error bars in all the bar graphs and line graphs represented SD. Shapiro-wilk test was employed to determine whether the data were normally distributed. The comparisons between two groups were evaluated by independent sample two-tails *t*-test. Three or more groups were evaluated by one-way ANOVA test. $^{*}P < 0.05$, $^{**}P < 0.01$, $^{***}P < 0.001$, and $^{****}P < 0.0001$.

3. Results and discussion

3.1. Synthesis and characterization of I_2@Nap-FFGP hydrogels

The synthesis of the self-assembling factor Nap-FFGP was straightforward and performed according to standard solid-phase peptide synthesis (SPPS) (Scheme S1 and Fig. S1A). Based on its established efficacy, diphenylalanine was included as an excellent self-assembly motif to design our target molecule. The N-terminal naphthalene (Nap) group, which exhibited strong π−π stacking interactions, significantly enhanced the self-assembly potential. Specifically, the C-terminal Pro (P), which is structurally analogous to pyrrolidone, was used to form a complex with iodine, yielding an iodine-containing peptide hydrogel.

A heating–cooling method was used to prepare the hydrogel. Nap-FFGP (3.0 mg/mL) was sufficient to form a self-supported hydrogel (inset in Fig. 1A); abundant nanofibers formed, as observed in its TEM image (Fig. 1A). Iodine was then incorporated into Nap-FFGP to form hydrogels and the iodine-incorporated samples are hereinafter referred to as I_2@Nap-FFGP. Incorporating iodine at Nap-FFGP to iodine ratios of 3:0.3 or 3:0.6 diminished assembly quality, resulting in sparse nanofibers and a lack of hydrogel formation. An increase in the ratio to 3:1 enhanced gelation without any notable morphological changes. However, in the I_2@Nap-FFGP sample with a ratio of 3:2, nanoparticles were observed in the TEM images alongside a visible precipitate in the hydrogel, which indicated that the saturation point in the peptide-iodine complexation was reached (Fig. 1A). A rheological test showed that the dynamic storage moduli (G′) of both the Nap-FFGP and I_2@Nap-FFGP hydrogels were nearly one order of magnitude higher than their loss moduli (G″). Additionally, the G′ and G″ values were independent with broad ranges of frequencies, confirming the formation of stable hydrogels of Nap-FFGP (3 mg/mL) and I_2@Nap-FFGP (3 mg/mL Nap-FFGP complexed with 1 mg/mL iodine) (Fig. 1B and Fig. S2). The critical micelle concentrations (CMCs) of Nap-FFGP and I_2@Nap-FFGP were 0.2677 and 0.4747 mg/mL, respectively, indicating that the addition of iodine impaired the assembly ability, in agreement with the optical and TEM images (Fig. 1C). We further measured and analyzed the secondary structure by circular dichroism (CD) spectra. After the addition of iodine, an increase of α-helix could be observed while proportion of β-sheet decreased in the I_2@Nap-FFGP hydrogel (Fig. S3). We finally chose the I_2@Nap-FFGP hydrogel with a ratio of 3:1 for subsequent tests, as it exhibited superior mechanical properties and optimal iodine loading to the other I_2@Nap-FFGP hydrogels.

Stability assessments of the I_2@Nap-FFGP hydrogels by injecting into a PBS buffer confirmed their structural integrity (Fig. 1D). Additionally, the I_2@Nap-FFGP hydrogel was subjected to alternating cycles of high and low strain at 25 °C. As shown in Fig. 1E and F, the G′ exceeded the G″ under low oscillatory strain (1 %), indicating a hydrogel status. Conversely, at high strain (100 %), the G′ declined to below the G″, indicating a rapid disruption of the gel and transition to a sol-like stage. The sol-like stage quickly reverted to the hydrogel state upon the oscillatory strain returning to 1 %. The modulus remained nearly constant over five cycles, indicating the exceptional self-healing ability of the I_2@Nap-FFGP hydrogel; this is suitable for applications that require shear-thinning hydrogels. However, compared to the I_2@Nap-FFGP hydrogel, the Nap-FFGP hydrogel displayed inferior self-healing capabilities. Subsequently, the release profile of iodine was measured and compared with that of the clinical agent PVP-I. As shown in Fig. 1G, the I_2@Nap-FFGP hydrogel allowed for the sustained and slow release of iodine, with approximately 80 % release over 24 h, in stark contrast to the near-complete (100 %) release of iodine from PVP-I within 2 h. This result indicates the potential of the designed I_2@Nap-FFGP hydrogel as an effective vehicle for continuous and sustained iodine delivery.

Further investigation into the role of the N-terminal Pro in iodine complexation was conducted by synthesizing a peptide, Nap-FFGA, with alanine substituting for Pro. Its synthesis was confirmed by liquid chromatography-mass spectrometry (Fig. S1B). A slight red shift was

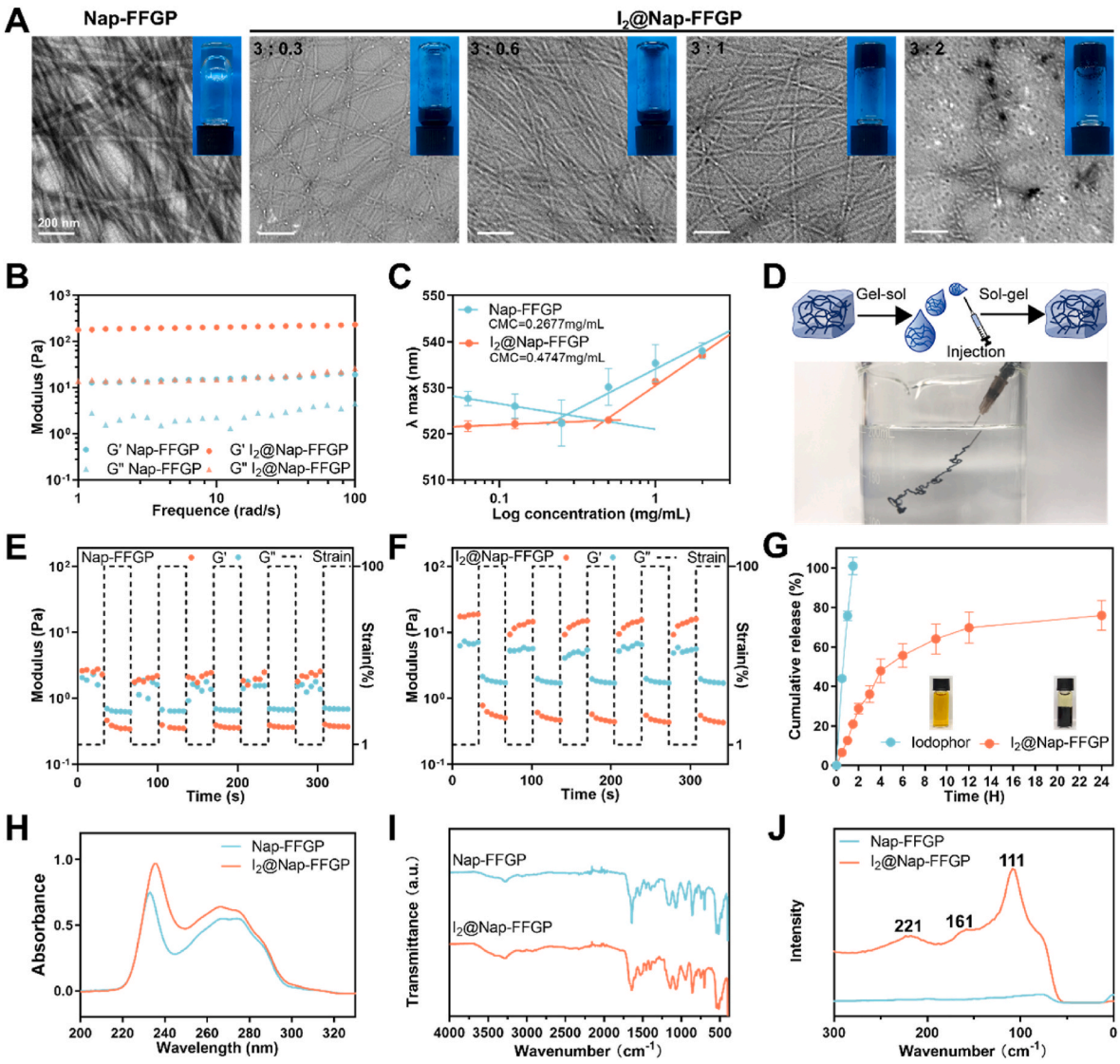

Fig. 1. Formation and characterization of I_2@Nap-FFGP. (A) TEM images of Nap-FFGP (3 mg/mL) and I_2@Nap-FFGP (the ratio of Nap-FFGP to iodine was 3:0.3, 3:0.6, 3:1, 3:2 respectively with optical images inserted). (B) Frequency sweep of the dynamic storage modulus (G′) and loss modulus (G″) of a Nap-FFGP and I_2@Nap-FFGP hydrogel. (C) CMC of Nap-FFGP and I_2@Nap-FFGP. n = 3. (D) The formation of the injectable I_2@Nap-FFGP hydrogel. The modulus of the (E) Nap-FFGP and (F) I_2@Nap-FFGP hydrogel under alternating cycles, where 100 % for high-shear strain and 1 % for low one. (G) The release profiles of iodine in I_2@Nap-FFGP hydrogel and iodophor. n = 3. (H) UV–vis spectrum of Nap-FFGP and I_2@Nap-FFGP. (I) ATR-FTIR spectrum of Nap-FFGP and I_2@Nap-FFGP. (J) Raman spectrum of Nap-FFGP and I_2@Nap-FFGP.

observed in its UV–Vis spectrum (Fig. 1H and S4) after it was complexed with iodine. We further conducted Fourier-transform infrared (FTIR) spectroscopy to investigate the interactions between Nap-FFGP and iodine. As illustrated in Fig. 1I, a subtle red shift of approximately 1640 cm^{-1}, attributed to ν(C=O), could be noted post iodine complexation, accompanied by a modest decrease in peak intensity, suggesting successful complexation of the carbonyl group (C=O) and iodine. Conversely, no significant changes were observed in the FTIR spectrum of the Nap-FFGA post iodine interaction, except for the disappearance of the absorption peak at 1750 cm^{-1}, which might indicate an interaction between iodine and the carboxyl group (Fig. S5). The Raman spectra of lyophilized powders of the solid iodine-containing peptide complexes revealed three distinct vibrational modes (Fig. 1J and S6). As the peak ascribed to free I_2 appears at 180 cm^{-1} in Raman spectra [24], the absence of a peak at 180 cm^{-1} for both I₂@Nap-FFGP and I₂@Nap-FFGA suggests that neither contained free iodine. The peak at approximately 160 cm^{-1} in the spectrum for I_2@Nap-FFGP might signify the symmetric stretching vibration of I_2 in its complexation state; this peak was not identifiable for I_2@Nap-FFGA. The peak at 111 cm^{-1} may correspond to the symmetric stretching vibration of $[I_3]^-$ while the peaks at 221 cm^{-1} might be double peaks, which might reveal the amino acid-iodine complex involved both amino and carboxyl groups [25,26]. Such results indicate that both complexed iodine and polyiodides were present in I_2@Nap-FFGP, whereas only polyiodides were maintained in I_2@Nap-FFGA [27]. Furthermore, I_2@Nap-FFGA failed to form a self-supported hydrogel (Fig. S7). Therefore, we found that the N-terminal Pro in the peptide facilitated strong iodine complexation and the formation of a stable iodine-containing hydrogel.

3.2. *Antibacterial effect of iodine-containing hydrogels*

To evaluate the antibacterial efficacy of I_2@Nap-FFGP, its effects on methicillin-resistant *Staphylococcus aureus* (MRSA) bacteria were assessed at concentrations at 3 mg/mL. The MRSA population was quantified using the plate counting method (Fig. 2A). All the iodine-complexed peptide hydrogels dramatically reduced MRSA populations

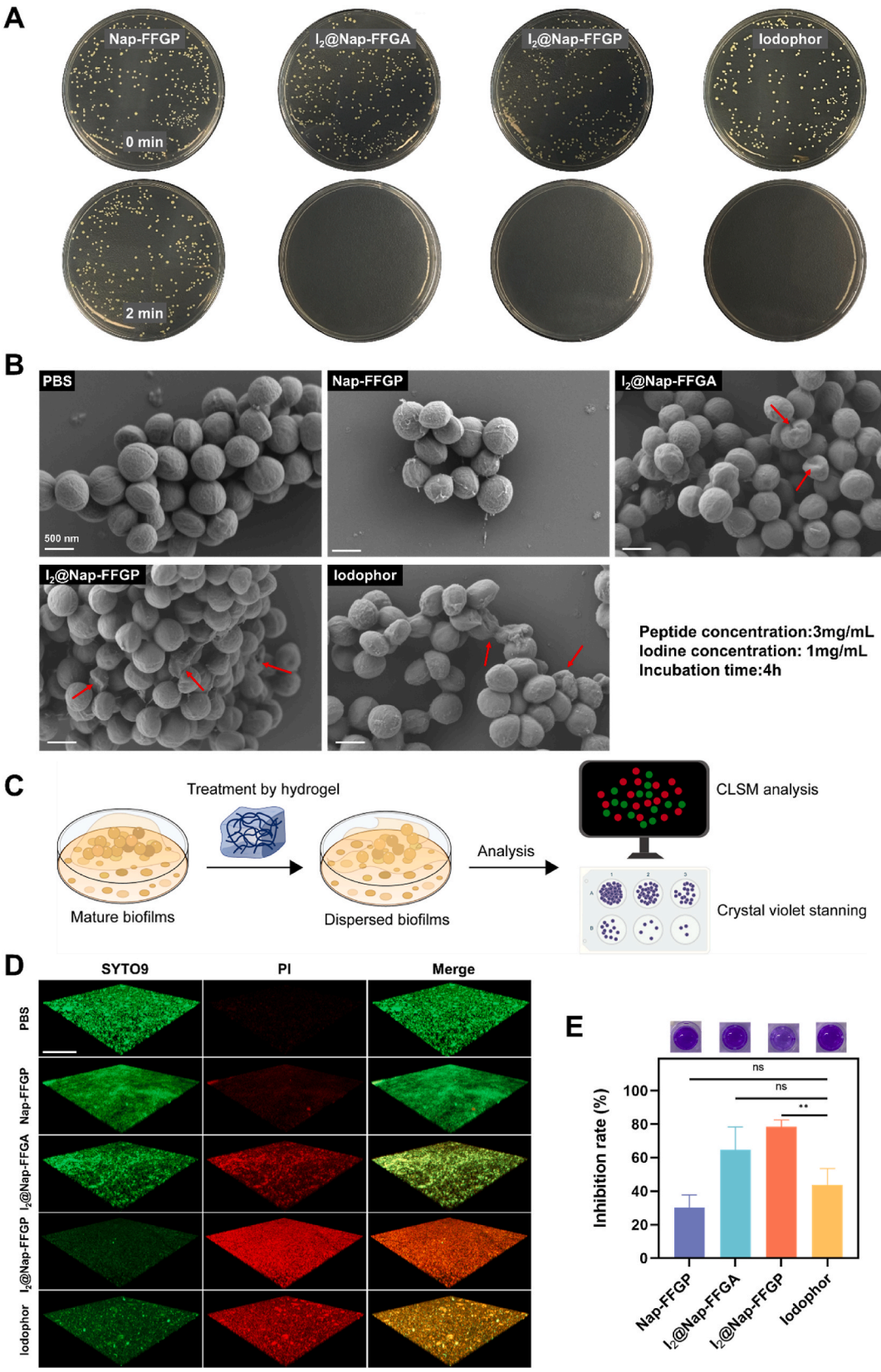

Fig. 2. Antibacterial effect of I_2@Nap-FFGP against MRSA. (A) The images of antibacterial effect of different treatments after 2 min by spread plate of MRSA. (B) SEM images of the morphological changes of MRSA incubated with different agents. (C) The design and process workflow of biofilm-related tests. (D) Representative 3D CLSM images of MRSA biofilm after different treatments. Live bacteria embedded in biofilms are represented as green fluorescent (labelled with SYTO9) and red fluorescent represented as dead bacteria (labelled with PI). Scale bars, 100 μm. (E) Crystal violet staining images and quantitative analyses of MRSA biofilm biomass after different treatment. All the data were presented as means ± SD, while n = 3. The significance was evaluated by one-way ANOVA test in (E). $^{**}P < 0.01$; n.s, not significant.

upon treatment, with no observable colonies remaining after only 2 min of exposure. We then studied the morphological changes in the MRSA bacteria using scanning electron microscopy (SEM). The wild-type MRSA bacteria maintained almost intact morphologies after treatment with PBS and Nap-FFGP despite the presence of the nanofibers. In contrast, when treated with the iodine-complexed hydrogels, the bacterial cells were deformed, collapsed, and rough, indicating substantial bacterial damage (Fig. 2B). Biofilm formations are vital to persistent bacterial infections, biofilms cause antibiotic resistance and protect bacteria from the host immune system. Therefore, the disruption of biofilms is challenging [28]. We further investigated the effects of I_2@Nap-FFGP on bacterial biofilms using 3D confocal laser scanning microscopy (CLSM) (Fig. 2D) and crystal violet staining (Fig. 2E) to quantify the biofilm clearance. Treatment with PBS resulted in minimal alterations of the biofilm, while treatment with Nap-FFGP caused only a slight reduction in optical density (OD595), which may be due to the absence of the antibacterial agent iodine. In contrast, treatment with I_2@Nap-FFGP resulted in strong red fluorescence and negligible green fluorescence, suggesting that I_2@Nap-FFGP exhibited enhanced biofilm permeation and substantial antibacterial efficacy. Furthermore, the OD595 decreased by approximately 80 % after treatment with I_2@Nap-FFGP, indicating significant biofilm ablation. Treatment with iodophor (PVP-I) also resulted in strong red and green fluorescence, but with less than a 50 % decrease in biofilm formation.

To investigate its ability of I_2@Nap-FFGP to induce outer membrane permeation, a lipophilic dye 1-(N-phenylamino)naphthalene (NPN) was utilized. NPN exhibits weak fluorescence in aqueous media and significantly higher fluorescence when interacting with lipidic bacterial cell membranes [29,30]. Furthermore, NPN cannot permeate through bacterial membranes unless the membranes are compromised or damaged. As shown in Fig. S8, MRSA exhibited a remarkable increase in fluorescence after treatment with Nap-FFGP, indicating that the permeability of the MRSA outer membranes was enhanced. These results suggest that Nap-FFGP, the skeleton of the I_2@Nap-FFGP hydrogel, might be a reinforcer of iodine permeation, resulting in I_2@Nap-FFGP exhibiting superior elimination of MRSA biofilms compared to PVP-I.

3.3. *In vitro* biocompatibility

Upon establishing the effective abolishment of bacteria by the I_2@Nap-FFGP hydrogel, we investigated its application in physiological humid and aqueous pathological conditions. We focused on endometritis, a common gynecological disease that is typically caused by bacterial infections [31,32], and often leads to chronic pelvic pain and ectopic pregnancy, and which is a prime cause of infertility [33,34]. We evaluated the biocompatibility of I_2@Nap-FFGP, as biosafety is as crucial as therapeutic efficacy when considering biomedical applications. Endometrial stromal cells were treated with I_2@Nap-FFGP or iodophor. Calcein-AM (green fluorescence) was used to identify live cells, whereas BOBO-3 iodide (red fluorescence) indicated dead cells. Bright-green fluorescence was observed after treatment with I_2@Nap-FFGP, indicating preserved cell viability, which was corroborated by cell proliferation results. Meanwhile, although the above results show that iodophor could remove bacterial biofilms, there was negligible green fluorescence and cell proliferation was almost completely inhibited (Fig. 3A and B). In addition, we performed a hemolysis test because I_2@Nap-FFGP is expected to come into contact with endometritis wounds, and thus may be exposed to blood. The results revealed

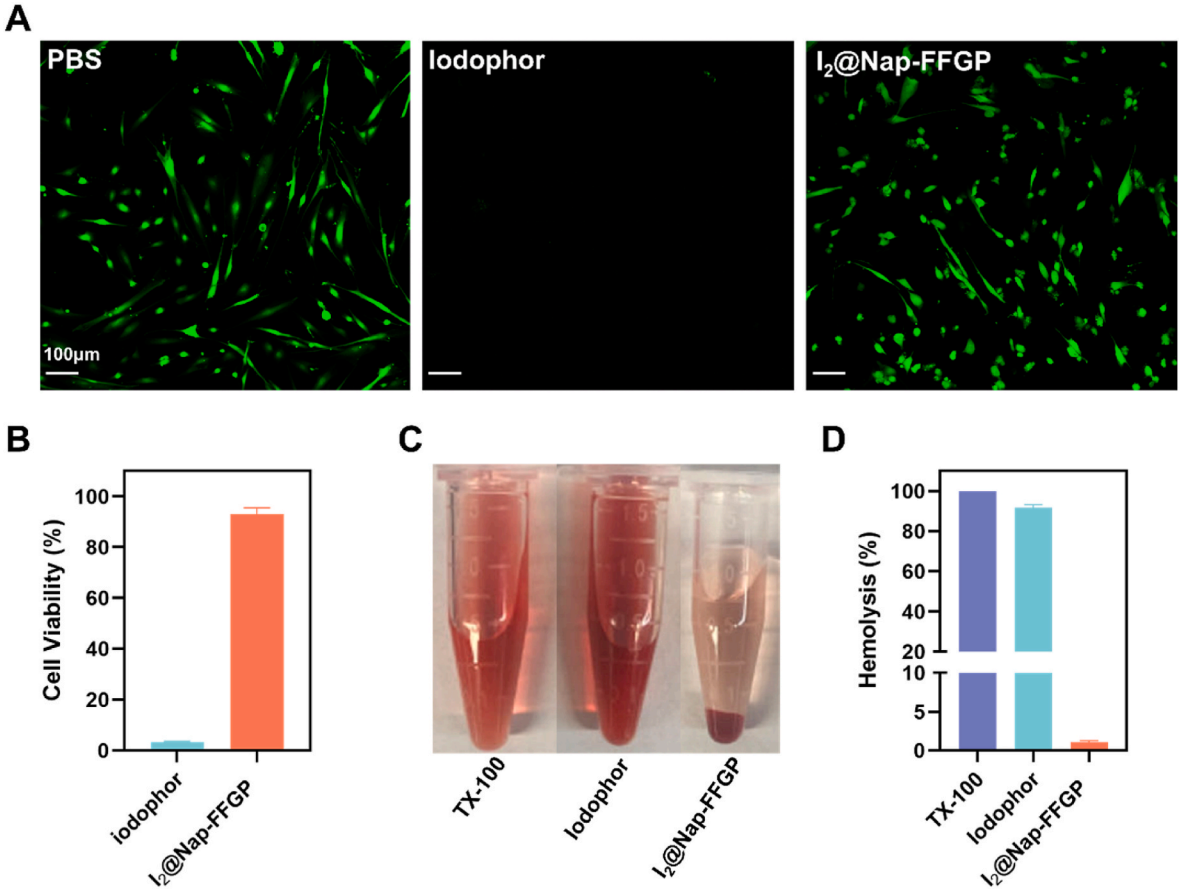

Fig. 3. The biocompability of I_2@Nap-FFGP *in vitro*. (A) CLSM images of endometrial stroma cells and (B) cell viability of endometrial stroma cells after treatment with iodophor and I_2@Nap-FFGP hydrogel. (C) Optical images and (D) hemolysis rate of mouse red blood cell treated with iodophor and I_2@Nap-FFGP hydrogel. All the data were presented as means ± SD, while n = 3.

that I_2@Nap-FFGP exhibited a low hemolysis ratio at the tested concentrations, whereas the iodophor caused severe hemolysis. Thus, I_2@Nap-FFGP demonstrated superior hemocompatibility (Fig. 3C and D). We then evaluated the *in vitro* degradation of the I_2@Nap-FFGP hydrogel in simulated uterine fluid. The hydrogel gradually turned into transparent and fluidity, together with the release of iodine. At day 10, the hydrogel was almost completely dissolved, indicating the biodegradability in physiological environments (Fig. S9). These *in vitro* results suggest that I_2@Nap-FFGP is a promising therapeutic option for treating endometritis *in vivo*.

3.4. In vivo repair of infection-based endometritis

To assess the *in vivo* therapeutic efficacy of the iodine-complexed hydrogel, a mouse model of MRSA infection-based endometritis was established. Thirty female mice were randomly divided into six groups of five. To induce infection, 60 μL of MRSA were injected into the uteri of mice in five groups, followed by treatment administration, while a sixth group of healthy mice was served as a control (Fig. 4A). The appearance of uterine tissues was assessed to evaluate inflammatory response. As shown in Fig. 4B, normal uterine tissues appeared pale yellow, while the PBS treatment group exhibited significant redness and swelling. Treatment with I_2@Nap-FFGA, Nap-FFGP, and iodophor resulted in varying improvements, with notable recovery observed in the Nap-FFGP and I_2@Nap-FFGA groups. I_2@Nap-FFGP demonstrated the highest recovery, with uterine tissues closely resembling healthy controls, indicating effective inflammation alleviation.

After euthanizing the mice, hematoxylin-eosin (HE) staining was used to analyze uterine and major organ histomorphologies. As shown in Fig. 4C, control mice exhibited intact, well-defined endometrial structures, while PBS treatment induced pathological changes such as loose tissue arrangement, increased interstitial spaces, hemorrhage, epithelial damage, and neutrophil infiltration. Minimal improvements followed Nap-FFGP and I_2@Nap-FFGA treatments, whereas I_2@Nap-FFGP treatment notably restored edema and stabilized tissue structures, indicating superior efficacy. Iodophor treatment provided partial recovery but induced higher inflammatory scores than I_2@Nap-FFGP (Fig. 4D) according to standard measurement protocol [35,36].

Pro-inflammatory cytokines IL-1β and TNF-α were quantified in uterine tissues using immunohistochemical (IHC) and immunofluorescence (IF) staining (Fig. 4G and Fig. S10), with results analyzed in Fig. 4E and F. IHC staining indicated reduced IL-1β and TNF-α levels in the Nap-FFGP and iodophor groups. Notably, IL-1β and TNF-α levels significantly decreased following I_2@Nap-FFGP treatment, reaching levels comparable to the healthy control group. Real-time qPCR analysis further showed significant down-regulation of TNF-α and IL-1β mRNA expression after I_2@Nap-FFGP treatment (Fig. S11).

To verify the potential toxicity of I_2@Nap-FFGP, H&E staining was performed to evaluate the morphological changes of major organs after different treatments. The treatment groups exhibited insignificant difference compared to healthy mice in heart, liver, spleen, lung and kidney, which indicated the biocompatibility of the employed treatments (Fig. S12). Collectively, these results suggest that I_2@Nap-FFGP not only mitigates pathogenic presence but also promotes endometrial repair, highlighting its potential as a fertility-restoration strategy.

3.5. Restored fertility of mice with endometritis after treatment with I_2@Nap-FFGP

After resolving inflammation and restoring the endometrium, we consequently investigated the therapeutic effect of I_2@Nap-FFGP on the restoration of fertility endometritis-affected mice. Angiogenesis in the endometrium is crucial for tissue reconstitution [37,38]. Accordingly, immunofluorescence staining for α-smooth muscle actin (α-SMA) and CD31 (an established angiogenesis biomarker) was performed. Colocalization of CD31 and α-SMA indicated sites of neovascularization (Fig. 5A). Following 24h treatment with I_2@Nap-FFGP, CD31-positive area and α-SMA-positive area were significantly higher than in other treatment groups (Fig. 5A and S13), indicating enhanced neovascularization. Vascular endothelial growth factor (VEGF) has been shown to repair damaged vessels and promote angiogenesis by enhancing vascular endothelial cell proliferation and migration in the later stages of healing [39]. Thus, VEGF expression was evaluated by immunohistochemical staining. As shown in Fig. S14, I_2@Nap-FFGP notably upregulated VEGF levels, aligning with CD31 results and supporting substantial vascularization and tissue regeneration in the uterine environment.

To assess reproductive function recovery, embryo numbers were evaluated in mice with endometritis (Fig. 5B and C). Endometritis significantly impaired pregnancy outcomes compared to healthy controls. The PBS treated group showed only a 20 % pregnancy rate, with reduced embryo numbers relative to controls. Nap-FFGP and I_2@Nap-FFGA treatments moderately improved pregnancy rates to approximately 45 % and 30 %, respectively. Importantly, I_2@Nap-FFGP, which demonstrated optimal endometrial restoration, significantly improved pregnancy rates and achieved embryo numbers comparable to those in the control group. These results verified the eradication of bacterial infection and effective endometrial repair by I_2@Nap-FFGP, which successfully reversed adverse pregnancy outcomes. Overall, treatment with I_2@Nap-FFGP markedly increased pregnancy rates, highlighting its therapeutic efficacy in endometrium restoration post-endometritis.

4. Conclusions

Iodine, recognized for its high efficacy and cost-effectiveness as an antiseptic, has been extensively employed in the clinical disinfection of the skin and mucous membranes because of its broad-spectrum antimicrobial properties and ease of application. However, the uncontrolled release of highly reactive and toxic iodine in physiologically and pathologically moist environments hinders its clinical application. In this study, we successfully demonstrated an iodine-containing peptide hydrogel optimized for humid and aqueous pathological conditions. The N-terminal-Pro–iodine complex stabilized I_2, enabling a sustainable release profile. This complex hydrogel demonstrated excellent biocompatibility, exceptional antibacterial activity and effectively disrupted biofilm formation. When used for treating infection-induced endometritis in mice, the iodine-complex hydrogel alleviated inflammation and facilitated endometrial repair. In addition, the hydrogel significantly restored the fertility of mice with endometritis. Therefore, the iodine–peptide complex hydrogel provides a potential therapeutic solution to meet the clinical demands for disinfecting bacteria and treating bacterial infections.

CRediT authorship contribution statement

Yu Zhang: Writing – original draft, Validation, Methodology, Investigation, Formal analysis. **Haiyan Liu:** Writing – original draft, Validation, Methodology, Investigation, Formal analysis. **Weiqi Zhang:** Validation, Methodology, Investigation. **Yinghao Ding:** Validation, Methodology, Investigation. **Shengyi Zhang:** Investigation. **Xiaowan Huang:** Investigation. **Jiali Chen:** Writing – review & editing, Writing – original draft, Supervision, Project administration, Data curation, Conceptualization. **Zhimou Yang:** Writing – review & editing, Supervision, Project administration, Funding acquisition, Data curation, Conceptualization. **Feng Lin:** Writing – review & editing, Supervision, Project administration, Funding acquisition, Data curation, Conceptualization.

Ethics approval and consent to participate

Animal experimental protocols were approved by the First Affiliated Hospital of Wenzhou Medical University (WYYY-AEC-2024-004).

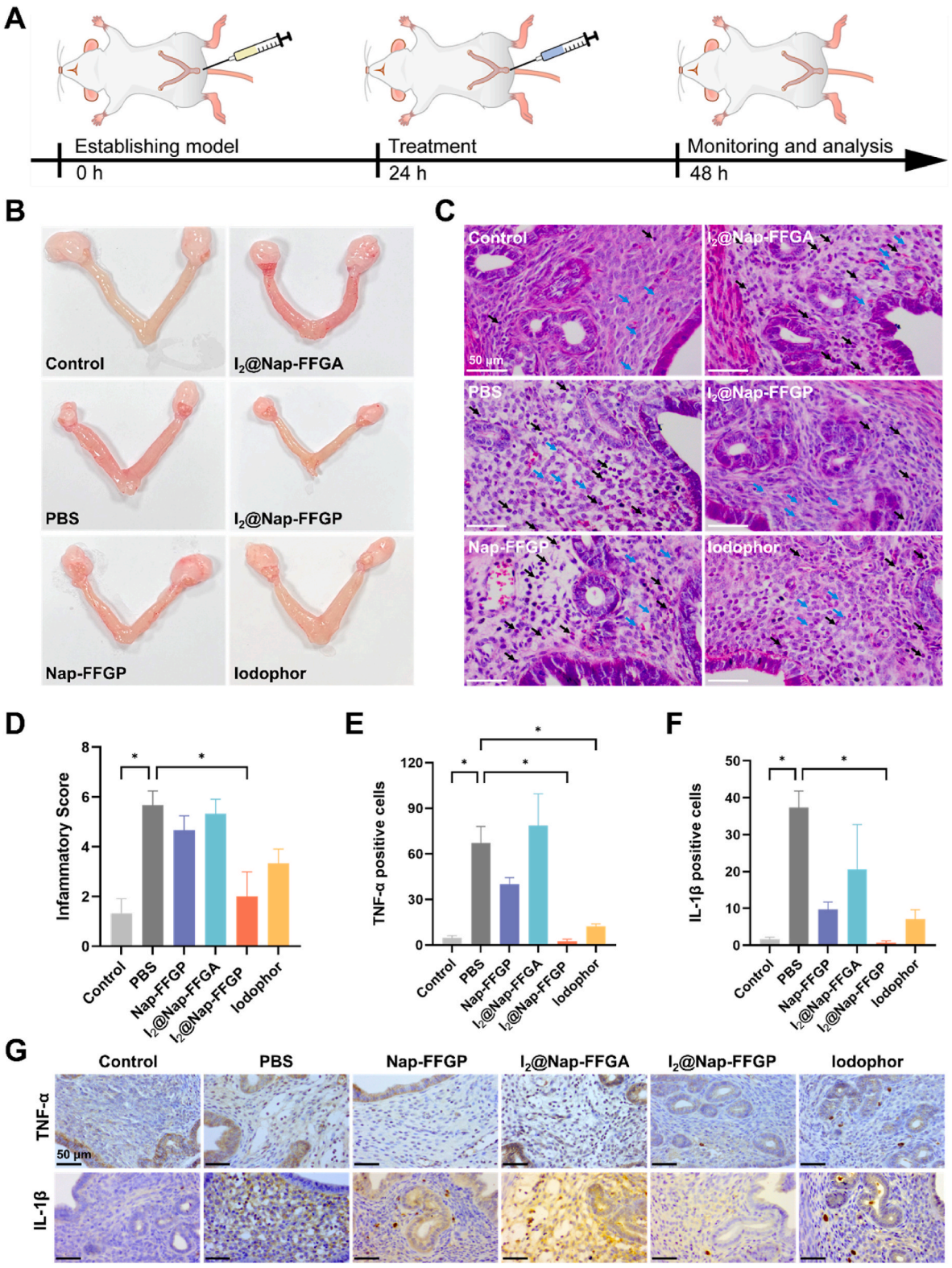

Fig. 4. *In Vivo* Therapy of Endometritis. (A) Schematic illustration of the protocol for establishing and treating endometritis in mice. (B) Optical images of uteri following different treatment. (C) H&E staining of uterine tissues and (D) quantification of inflammatory scores for each group, blue arrows indicate resident interstitial cells, and black arrows indicate neutrophil. (E–F) Quantitative analysis of TNF-α (E) and IL-1β (F) levels in uterine tissues following different treatment. (G) Representative images of immunohistochemical staining for TNF-α and IL-1β in uterine tissues following different treatment, Scale bars = 50 μm. Data are presented as mean ± SD, n = 3 per group. Statistical significance was determined using one-way ANOVA for panels (D), (E), and (F); *P < 0.05.

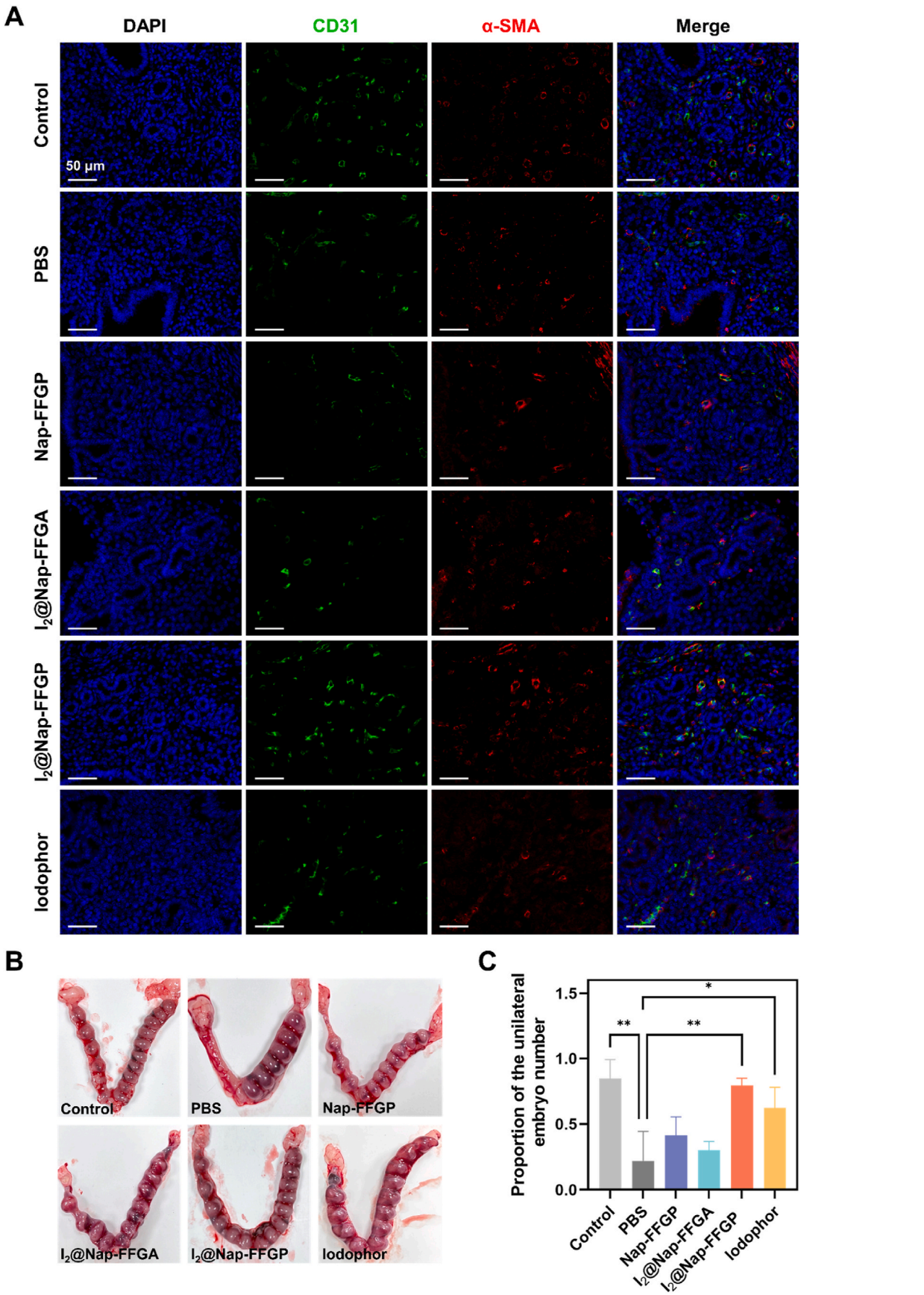

Fig. 5. Amelioration of endometrial receptivity of endometritis. (A) Immunofluorescence staining images of CD31(green) and α-SMA (red) in uterine tissues. (B) Representative images of uteri with implantation sites on pregnancy day 15. (C) Quantitative analysis of embryo numbers in the endometrium among different treatment groups. All the data were presented as means ± SD, n = 3. The significance was evaluated by one-way ANOVA test in (B). *P < 0.05; **P < 0.01.

Declaration of competing interest

The authors declare that they have no known competing financial interests or personal relationships that could have appeared to influence the work reported in this paper.

Acknowledgements

This work was supported by funding from the National Natural Science Foundation of China (81921004), Discipline Cluster of Oncology of Wenzhou Medical University (z1-2023007) and Zhejiang Provincial Natural Science Foundation of China (LBY24H040012)

Appendix A. Supplementary data

Supplementary data to this article can be found online at https://doi.org/10.1016/j.bioactmat.2025.01.010.

References

[1] D. Ristic-Medic, Z. Piskackova, L. Hooper, J. Ruprich, A. Casgrain, K. Ashton, M. Pavlovic, M. Glibetic, Methods of assessment of iodine status in humans: a systematic review, Am. J. Clin. Nutr. 89 (2009) 2052S–2069S.
[2] A.M. Leung, L.E. Braverman, Consequences of excess iodine, Nat. Rev. Endocrinol. 10 (2014) 136–142.
[3] J. Chang, G. Zhao, X. Zhao, C. He, S. Pang, J.n.M. Shreeve, New promises from an old friend: iodine-rich compounds as prospective energetic biocidal agents, Acc. Chem. Res. 54 (2020) 332–343.
[4] D.H. Kang, C. Ma, N.G. Park, Antiseptic povidone–iodine heals the grain boundary of perovskite solar cells, ACS Appl. Mater. Interfaces 14 (2022) 8984–8991.
[5] T. Gillam, C. Goh, N. Ninan, K. Bilimoria, H. Shirazi, S. Saboohi, S. Al-Bataineh, J. Whittle, A. Blencowe, Iodine complexed poly (vinyl pyrrolidone) plasma polymers as broad-spectrum antiseptic coatings, Appl. Surf. Sci. 537 (2021) 147866.
[6] Y. Chen, Y. Yang, Q. Liao, W. Yang, W. Ma, J. Zhao, X. Zheng, Y. Yang, R. Chen, Preparation, property of the complex of carboxymethyl chitosan grafted copolymer with iodine and application of it in cervical antibacterial biomembrane, Mater. Sci. Eng., C 67 (2016) 247–258.
[7] Q. Song, Z. Xiao, T. Liu, H. Gao, X. Chen, Q. Jia, P. Li, D. Wei, Antibacterial iodine-releasing coatings of cross-linked poly (N-vinylpyrrolidone) synthesized by solvent-free initiated chemical vapor deposition, ACS Macro Lett. 13 (2024) 1056–1064.
[8] A.F. Widmer, A. Atkinson, S.P. Kuster, A. Wolfensberger, S. Klimke, R. Sommerstein, F.S. Eckstein, F. Schoenhoff, G. Beldi, C.A. Gutschow, Povidone iodine vs chlorhexidine gluconate in alcohol for preoperative skin antisepsis: a randomized clinical trial, JAMA 332 (2024) 541–549.
[9] P. Durani, D. Leaper, Povidone–iodine: use in hand disinfection, skin preparation and antiseptic irrigation, Int. Wound J. 5 (2008) 376–387.
[10] A.K. Balin, L. Pratt, Dilute povidone-iodine solutions inhibit human skin fibroblast growth, Dermatol. Surg. 28 (2002) 210–214.
[11] W. Sun, Z.X. Wang, Y. Guo, C. Li, G. Gao, F.G. Wu, Iodine/soluble starch cryogel: an iodine-based antiseptic with instant water-solubility, improved stability, and potent bactericidal activity, Carbohydr. Polym. 340 (2024) 122217.
[12] J.M.V. Makabenta, A. Nabawy, C.H. Li, S. Schmidt-Malan, V.M. Rotello, Nanomaterial-based therapeutics for antibiotic-resistant bacterial infections, Nat. Rev. Microbiol. (2020) 1–14.
[13] D. Chen, Z. Zhou, N. Kong, T. Xu, J. Liang, P. Xu, B. Yao, Y. Zhang, Y. Sun, Y. Li, B. Wu, X. Yang, H. Wang, Inhalable SPRAY nanoparticles by modular peptide assemblies reverse alveolar inflammation in lethal Gram-negative bacteria infection, Sci. Adv. 10 (2024) eado1749.
[14] T. Gao, H. Fan, X. Wang, Y. Gao, W. Liu, W. Chen, A. Dong, Y.J. Wang, Povidone–iodine-based polymeric nanoparticles for antibacterial applications, ACS Appl. Mater. Interfaces 9 (2017) 25738–25746.
[15] J. Fonseca, M. Cano-Sarabia, P. Cortés, J. Saldo, D. Montpeyó, J. Lorenzo, M. Llagostera, I. Imaz, D. Maspoch, Metal-organic framework-based antimicrobial touch surfaces to prevent cross-contamination, Adv. Mater. (2024) 2403813.
[16] Y. Li, Z. Yang, Q. Sun, R. Xu, R. Li, D. Wu, R. Huang, F. Wang, Y. Li, Biocompatible cryogel with good breathability, exudate management, antibacterial and immunomodulatory properties for infected diabetic wound healing, Adv. Sci. 10 (2023) 2304243.
[17] Y. You, Y.X. Zhu, J. Jiang, Z. Chen, C. Wu, Z. Zhang, H. Lin, J. Shi, Iodinene nanosheet-to-iodine molecule allotropic transformation for antibiosis, J. Am. Chem. Soc. 145 (2023) 13249–13260.
[18] A. Levin, T.A. Hakala, L. Schnaider, G.J. Bernardes, E. Gazit, T.P. Knowles, Biomimetic peptide self-assembly for functional materials, Nat. Rev. Chem 4 (2020) 615–634.
[19] H. Zhu, H. Wang, B. Shi, L. Shangguan, F. Huang, Supramolecular peptide constructed by molecular Lego allowing programmable self-assembly for photodynamic therapy, Nat. Commun. 10 (2019) 2412.
[20] Z. Wang, H. Luo, H. Wang, M. Xiao, H. Jia, C. Ren, J. Liu, Peptide-based supramolecular therapeutics for fighting major diseases, Adv. Funct. Mater. (2024) 2314492.
[21] M.H. Sangji, S.R. Lee, H. Sai, S. Weigand, L.C. Palmer, S.I. Stupp, Self-sorting vs coassembly in peptide amphiphile supramolecular nanostructures, ACS Nano 18 (2024) 15878–15887.
[22] S. Adorinni, S. Gentile, O. Bellotto, S. Kralj, E. Parisi, M.C. Cringoli, C. Deganutti, G. Malloci, F. Piccirilli, P. Pengo, Peptide stereochemistry effects from p K a-shift to gold nanoparticle templating in a supramolecular hydrogel, ACS Nano 18 (2024) 3011–3022.
[23] M. Gosecka, M. Gosecki, D. Jaworska-Krych, Hydrophobized hydrogels: construction strategies, properties, and biomedical applications, Adv. Funct. Mater. 33 (2023) 2212302.
[24] E. Wulandari, K. Bilimoria, M. Krasowska, S. Al-Bataineh, D. Beattie, T. Gillam, W. Ge, J.D. Whittle, E.H. Wong, A. Blencowe, Nanoscale iodophoric poly (vinyl amide) coatings for the complexation and release of iodine for antimicrobial surfaces, Appl. Surf. Sci. 641 (2023) 158422.
[25] S. Zhang, C. Kai, B. Liu, S. Zhang, W. Wei, X. Xu, Z. Zhou, Facile fabrication of cellulose membrane containing polyiodides and its antibacterial properties, Appl. Surf. Sci. 500 (2020) 144046.
[26] A.M. Petrosyan, G. Giester, G.S. Tonoyan, V.V. Ghazaryan, A.L. Zatikyan, R. Yu Chilingaryan, A.A. Margaryan, A.H. Mkrtchyan, Iodides and polyiodides of L-arginine, J. Mol. Struct. 1321 (2025) 139688.
[27] X. Xu, Y. Guan, Investigating the complexation and release behaviors of iodine in Poly (vinylpyrrolidone)-Iodine systems through experimental and computational approaches, Ind. Eng. Chem. Res. 59 (2020) 22667–22676.
[28] S. Darvishi, S. Tavakoli, M. Kharaziha, H.H. Girault, C.F. Kaminski, I. Mela, Advances in the sensing and treatment of wound biofilms, Angew. Chem. Int. Ed. 134 (2022) e202112218.
[29] M.D. Torres, M.C. Melo, L. Flowers, O. Crescenzi, E. Notomista, C. de la Fuente-Nunez, Mining for encrypted peptide antibiotics in the human proteome, Nat. Biomed. Eng. 6 (2022) 67–75.
[30] A.W. Simonson, A.S. Mongia, M.R. Aronson, J.N. Alumasa, D.C. Chan, A. Lawanprasert, M.D. Howe, A. Bolotsky, T.K. Mal, C. George, Pathogen-specific antimicrobials engineered de novo through membrane-protein biomimicry, Nat. Biomed. Eng. 5 (2021) 467–480.
[31] J.M. Wessels, M.A. Domínguez, N.A. Leyland, S.K. Agarwal, W.G. Foster, Endometrial microbiota is more diverse in people with endometriosis than symptomatic controls, Sci. Rep. 11 (2021) 18877.
[32] P. Venkatesan, Bacterial infection linked to endometriosis, Lancet Microbe 4 (2023) e768.
[33] C. Chapron, L. Marcellin, B. Borghese, P. Santulli, Rethinking mechanisms, diagnosis and management of endometriosis, Nat. Rev. Endocrinol. 15 (2019) 666–682.
[34] X. Liu, S. Yan, H. Wu, M. Chen, H. Dai, Z. Wang, M. Chai, Q. Hu, D. Li, L. Chen, Interventional hydrogel microsphere controlled-releasing curcumin for photothermal therapy against endometriosis, Adv. Funct. Mater. (2024) 2315907.
[35] R.R. Vieira, R.A. da Silva, G.R. Sasso, P.C. Franco, F.T. Borges, P.D. Lima, J. M. Sanches, C.D. Gil, A.A. Carbonel, Lack of annexin a1 exacerbates inflammatory response in acute endometritis model, Inflammation 47 (2024) 1041–1052.
[36] M.P. Corrêa, R.D. Correia-Silva, G.R.S. Sasso, S.C. D'Ávila, K.V. Greco, S.M. Oliani, C.D. Gil, Expression pattern and immunoregulatory roles of Galectin-1 and Galectin-3 in atopic dermatitis and psoriasis, Inflammation (2022) 1133–1145.
[37] S. Zhang, E. Jia, W. Zhang, Z. Wang, D. Deng, Y. Zhang, X. Huang, Q. Tian, Y. Tan, B. Wang, Injectable alginate-based zwitterionic hydrogels promoting endometrial repair and restoring fertility, Int. J. Biol. Macromol. 275 (2024) 133458.
[38] X. Lv, W. Niu, B. Zhang, J. Chen, S. Yang, Y. Xue, Y. Dong, P. Yuan, Y. Pan, J. Tan, Self-assembled peptide hydrogels loaded with umbilical cord-derived mesenchymal stem cells repairing injured endometrium and restoring fertility, Adv. Healthcare Mater. (2024) 2400524.
[39] W. Zhang, W. Liu, L. Long, S. He, Z. Wang, Y. Liu, L. Yang, N. Chen, C. Hu, Y. Wang, Responsive multifunctional hydrogels emulating the chronic wounds healing cascade for skin repair, J. Contr. Release 354 (2023) 821–834.